Speciation controls on Ni adsorption to birnessite and organo-birnessite

Lena Chen [*], William B. Homoky, Caroline L. Peacock

School of Earth and Environment, University of Leeds, Leeds, UK

ARTICLE INFO

ABSTRACT

Nickel (Ni) is an essential micronutrient for phytoplankton. Its importance to both the modern and ancient Earth system has encouraged development of Ni and its isotopes as biogeochemical tracers. To interpret these signatures however, understanding of how Ni and its isotopes are recorded in marine archives is required. Here we simulate different inorganic and organic Ni species in seawater and investigate their adsorption behaviours to variably crystalline phyllomanganates and organo-mineral phyllomanganate. We conduct pH adsorption edge experiments to determine the binding affinity of the different Ni species to the minerals and then perform desorption experiments to operationally define Ni bonding strength. We also use thermodynamic surface complexation modelling to constrain Ni adsorption mechanisms. From the adsorption edges and stability constants generated from our modelling, the binding affinity increases in the order of Ni-formate$^+$ (aq) < NiCl$^+$ (aq) < Ni^{2+} (aq). From the desorption experiments, desorption at pH 8 is non quantitative and increases in the opposite order of Ni-formate$^+$ (aq) > NiCl$^+$ (aq) ~ Ni^{2+} (aq). For the organo-mineral however, Ni desorption at pH 8 is non quantitative and similar for all three experiments, and is significantly higher compared to the variably crystalline phyllomanganates. Although both our adsorption and desorption experiments were performed over 48 h, it is possible that desorption is somewhat slower than adsorption such that a longer desorption period may result in further Ni loss to solution and thus greater adsorption reversibility. Taken together however, the Ni-formate$^+$ (aq) and Ni organo-birnessite desorption experiments suggest that Ni bonding strength is decreased by the presence of organic carbon, compared to NiCl$^+$ (aq) and Ni^{2+} (aq). Because bonding strength governs equilibrium stable isotope fractionation, we use our experimental findings to suggest how Ni speciation in seawater might influence Ni isotope behaviour during adsorption to phyllomanganate. We find that our suggestions are consistent with isotopic measurements from natural sediments. Although the balance of Ni adsorption versus incorporation during uptake to phyllomanganates may play a greater part in explaining the variation in the Ni isotope composition in Mn-rich sediments, Ni speciation and the presence of organics might increase the range of δ^{60}Ni values measured in natural settings.

1. Introduction

In the oceans Ni is an important micronutrient. It is involved in a diverse range of biogeochemical processes for all forms of life because it is an essential component in multiple enzymes (reviewed in Ragsdale, 2009). Most notably, in phytoplankton Ni is a co-factor in the enzyme urease, which catalyses the decomposition of urea to ammonia. In marine cyanobacteria and prokaryotes, Ni forms part of the enzyme superoxide dismutase and Ni-Fe hydrogenases, used for cellular oxidative defence and nitrogen fixation (Barondeau et al., 2004; Dupont et al., 2010). It is also a vital component in the enzyme methyl-CoM reductase, which catalyses the production of methane (Jaun and Thauer, 2007). The bioavailability of Ni in the modern ocean is therefore essential for

the regulation of atmospheric CO$_2$ (Anbar, 2008), and decreasing bioavailability of Ni in the late Archean is thought to play a role in the evolution of Earth's atmosphere, from being methane dominant to more oxygen-rich (Konhauser et al., 2015; Konhauser et al., 2009; Wang et al., 2019). Ni and its isotopes in marine archives therefore have the potential to trace these key biogeochemical processes in the marine environment (Cameron et al., 2009; Wang et al., 2019).

For Ni and its isotopes to be useful proxies of past biogeochemical processes, understanding of its modern biogeochemical cycling together with its preservation in marine sediment archives is first required (Homoky et al., 2016; Horner et al., 2021). Recent work sheds new light on the potential controls of the modern distribution of Ni in the ocean and its oceanic budget (Fleischmann et al., 2023; Gueguen and Rouxel,

2021; John et al., 2022; Lemaitre et al., 2022; Little et al., 2020). The largest sediment sink for Ni is in oxic sediments but these deposits exhibit a huge range of isotopic compositions (reported in δ^{60}Ni notation, the parts per thousand deviation of the ^{60}Ni/^{58}Ni ratio from NIST SRM986) from −1.49 to +2.47 ‰ (Fleischmann et al., 2023; Gall et al., 2013; Gueguen et al., 2021; Gueguen et al., 2016; Gueguen and Rouxel, 2021; Little et al., 2020), which suggests that a number of processes must control Ni isotope variations in these oxic settings that are not yet understood.

In oxic settings, Ni is taken up by dispersed Fe-Mn (oxyhydr)oxide phases and deposited in oxic sediments. In Fe-Mn crusts and nodules, Ni is shown to be exclusively associated with the Mn-rich phase (Atkins et al., 2016). These phases are comprised of poorly but variably crystalline phyllomanganate, from vernadite which has turbostratic phyllomanganate layers (where the basal planes are out of alignment, and which is also usually intermixed with Fe (oxyhydr)oxides, and often interchangeably referred to as δMnO$_2$, a synthetic analogue) to c-disordered birnessite (where c-disordered describes the incoherently stacked phyllomanganate layers) (Peacock and Sherman, 2007a). To date, all Ni adsorption studies with variably crystalline phyllomanganate investigate the adsorption of the free aquo cation Ni^{2+} (aq) (Peacock and Sherman, 2007a; Peña et al., 2010; Sorensen et al., 2020). Through spectroscopy methods, Ni^{2+} (aq) is shown to adsorb to the mineral surface above/below vacancy sites in the phyllomanganate layers (Peacock and Sherman, 2007a; Peña et al., 2010; Sorensen et al., 2020) and then at seawater pH and with increasing time it is incorporated into the mineral structure (Peacock, 2009). In short duration experiments (up to ~48 h) there is negligible incorporation into the mineral structure (Peacock and Sherman, 2007a; Peacock, 2009). During adsorption to the surface, after 24 h the mineral-associated Ni is enriched in lighter isotopes with a Ni isotope fractionation ranging from Δ^{60}Ni$_{\text{mineral-aqueous}}$ = −2.76 to −3.35 ‰ (Δ^{60}Ni$_{\text{mineral-aqueous}}$ = δ^{60}Ni$_{\text{mineral}}$ − δ^{60}Ni$_{\text{aqueous}}$; Sorensen et al., 2020), which is much larger than the isotopic fractionation observed between the oxic sediment sink and seawater. This measured fractionation, however, may not be reflective of equilibrium conditions likely occurring in the ocean.

During equilibrium isotope fractionation, stable isotope theory predicts that bonding strength and isotopic behaviour are related, such that bonding environments that provide the highest bonding strength will concentrate the heaviest isotopes (e.g., Schauble, 2004). The bonding strength of Ni for variably crystalline phyllomanganate and consequently the isotopic composition of Ni drawn into the oxic sediment sink therefore might be influenced by several physiochemical factors. Notably, inorganic Ni in seawater is present as NiCl$^+$ and NiCl$_2$ (34%) in addition to Ni^{2+} (47%) (Turner et al., 1981), while a significant but variable proportion of Ni is also bound to organic ligands (Turner and Martino, 2006; Vraspir and Butler, 2009). Theoretical calculations and experiments show that the major species of Ni present in seawater are isotopically fractionated (Fujii et al., 2011) and recent studies suggest that the preferential uptake of isotopically heavy Ni species may help explain the heavy isotope signature of Mn-rich sediments (Gueguen et al., 2021; Sorensen et al., 2020). Ni-organic ligands could also influence the isotope composition of Mn-rich sediments and Fe-Mn crusts. Studies have yet to investigate whether different inorganic and organic Ni species have differing bonding strengths for phyllomanganate, that in turn might influence the Ni isotope composition of the mineral phase. Additionally given the variably crystalline phyllomanganates present in Fe-Mn (oxyhydr)oxides (Manceau et al., 2014; Peacock and Sherman, 2007b), which also include those associated with extracellular polymeric substances and bacterial cells to form organo-mineral assemblages (Toner et al., 2005a), different inorganic and organic Ni species may also have differing bonding strengths for various phyllomanganates, that may similarly influence the Ni isotope composition of the mineral phase.

In this study, we aim to shed light on how Ni speciation and phyllomanganate mineralogy controls Ni bonding strength, and in turn, how

this Ni bonding strength may influence Ni isotope fractionation during uptake from seawater to the oxic sediment sink. We use an experimental approach to investigate the adsorption of different inorganic and organic Ni species to variably crystalline phyllomanganates and organo-mineral phyllomanganate. We adsorb the inorganic Ni species Ni^{2+} and NiCl$^+$ and the organic Ni species Ni-formate$^+$ to δMnO$_2$, c-disordered birnessite and organo-mineral c-disordered birnessite. We use the monocarboxylic formic acid as an organic ligand and prepare organo-mineral c-disordered birnessite by adsorbing a tricarboxylic acid to c-disordered birnessite. Short-chain carboxylic acids and other low molecular weight organic acids are key intermediaries in the remineralisation of organic carbon and are thus prevalent in the marine environment (Barcelona, 1980) and might serve as simple model organic compounds for more complex forms of natural organic matter, which comprise a number of universal molecular structures containing predominantly carboxyl and hydroxyl groups (Zark and Dittmar, 2018). Furthermore organo-minerals contain a variety of reactive organic functional groups, such as COOH, CHOH, PO$_4$H$_3$, SH and NH$_2$ (Jiang et al., 2004; Merroun et al., 2011; Toner et al., 2005b; Warren and Haack, 2001), where the carboxyl group in particular is often responsible for trace metal binding (Boonfueng et al., 2009; Fariña et al., 2018; Moon and Peacock, 2012). We conduct pH adsorption edge experiments to determine the binding affinity of the different Ni species to the minerals, and then perform desorption experiments to operationally define Ni bonding strength, together with thermodynamic surface complexation modelling to constrain Ni adsorption mechanisms. Our primary objectives are to (1) determine whether and how Ni speciation and mineral crystallinity affects Ni adsorption to and desorption from phyllomanganates; (2) investigate the influence of organic carbon as an organic ligand or an organo-mineral on Ni adsorption to phyllomanganates; (3) suggest how Ni speciation and phyllomanganate mineralogy might influence Ni isotope behaviour during adsorption to phyllomanganate in the oxic sediment sink.

2. Methods

2.1. Synthesis of δMnO$_2$, c-disordered birnessite and organo-mineral c-disordered birnessite

δMnO$_2$ and c-disordered birnessite were synthesised following the redox method of Villalobos et al., (2003). To produce δMnO$_2$, 1280 mL of a 0.19 M KMnO$_4$ solution was added slowly (5 min total time) to 1440 mL of a 0.48 M NaOH solution whilst stirring vigorously. Then 1280 mL of a 0.29 M MnCl$_2$.4H$_2$O solution was added slowly (35 min total time) to the previously prepared mixed solution of KMnO$_4$ and NaOH whilst stirring vigorously at room temperature (Villalobos et al., 2003). The production of c-disordered birnessite is almost identical to the method for δMnO$_2$ except for the lower ratio of Mn(VII)/Mn(II) used during the precipitation. To produce c-disordered birnessite, 320 mL of a 0.196 M KMnO$_4$ solution was added slowly to 360 mL of a 0.51 M NaOH solution whilst stirring vigorously. Then 320 mL of a 0.366 M MnCl$_2$ solution was added slowly into the above mixture whilst stirring vigorously at room temperature. The suspensions were left to settle for ~4 h and then transferred into 250 mL Polypropylene copolymer (PPCO) centrifuge bottles and centrifuged at 2750g for 30 min. The supernatants were discarded. The slurries were then washed 5 times by mixing with 1 M NaCl and centrifuging at 2750g for 20 min. After each wash the supernatants were discarded. The last wash was adjusted to pH 8 and shaken overnight. The slurries were then washed 10 times by mixing with ultrapure water (18.2 MΩ.cm) and centrifuging at 3200g for 10 min. After each wash the supernatants were discarded. The slurries were then dialysed in Fisher regenerated cellulose membrane bags and placed in 4 L receptacles filled with ultrapure water. The water was replaced every day for 3 days. The final density of the δMnO$_2$ suspension was 20 g L^{-1}. The final density of the c-disordered birnessite suspension was 40 g L^{-1}.

An organo-mineral c-disordered birnessite was made following the

method of Zhang et al. (2021) by adding 5.5 g of 1,2,4 butane tricarboxylic acid to 0.2 g of the c-disordered birnessite in 200 mL 0.1 M NaCl and gently agitating for 48 h. The pH was adjusted to 8.5 using NaOH. The suspension was centrifuged and the supernatant was discarded. The slurry was rinsed with ultrapure water to remove tricarboxylic acid in the residual supernatant and loosely-bound tricarboxylic acid from the mineral. An aliquot of the slurry was dried at 30 °C and the carbon content was measured with a LECO SC144DR analyser. The synthesised mineral contained 1.4 wt% C.

The identity and crystallinity of the minerals were confirmed with X-ray diffraction (Supplementary Fig. A1). An aliquot of the slurry was dried in an oven at 30 °C and crushed into a fine powder using a pestle and mortar. The samples were analysed with a Bruker D8 X-ray diffractometer equipped with CuKα radiation (λ = 1.5418) and a LynxEye detector. Samples were analysed over 2–86° 2θ range with a 0.01° 2θ step size and 1085 ms acquisition time. The specific surface area of the minerals was measured using the BET-N_2 method with a Micromeritics Gemini VII. Aliquots of the minerals were degassed overnight with N_2 at 20 °C using a Flowprep060. The measured specific surface area for the δMnO$_2$, c-disordered birnessite and organo-birnessite are 188, 148 and 166 m^2g^{-1} respectively, where the error is ±5% of the reported value.

2.2. pH adsorption edge experiments

pH adsorption edge experiments were conducted with initial added Ni concentration at 2 μM Ni in background electrolytes of either 0.1 M NaCl, 0.7 M NaCl or 0.1 M NaCl with 0.1 M Na-formate. The experimental aqueous speciation of Ni as a function of pH was calculated with PHREEQC (Park and Kwon, 2021) using the stability constants from the MINTEQ.V4 database (Charlton and Parkhurst, 2002, modified for ionic strength using the Davies equation) (Supplementary Fig. A2). In 0.1 M NaCl background electrolyte, from pH 2 to 9, initial added Ni was present as ~90% Ni^{2+} (aq) with ~10% $NiCl^+$ (aq) (hereafter the Ni^{2+} (aq) adsorption experiments). In 0.7 M NaCl background electrolyte, from pH 2 to 9, initial added Ni was present as ~70% Ni^{2+} (aq) with ~30% $NiCl^+$ (aq), closely matching inorganic Ni speciation in seawater (Turner et al., 1981) (hereafter the $NiCl^+$ (aq) adsorption experiments). In 0.1 M NaCl with 0.1 M Na-formate background electrolyte, from pH 4 to 9, initial added Ni was present as ~67% Ni^{2+} (aq) with ~28% Ni-formate$^+$ (aq) and ~5% $NiCl^+$ (aq), representing a significant proportion of Ni bound to organic ligands (Turner and Martino, 2006; Vraspir and Butler, 2009) (hereafter the Ni-formate$^+$ (aq) adsorption experiments).

Batch pH adsorption edge experiments were conducted in 250 mL centrifuge bottles by adding 118 μL of 0.003 M Ni(NO$_3$)$_2$·6H$_2$O stock solution to 0.01 g of mineral in 199.6 mL of background electrolyte. Solid solution ratio was 0.05 g L^{-1}. The initial pH was measured and adjusted over pH 2 to 9 via the drop-wise addition of dilute HCl or NaOH. All pH measurements were calibrated to ±0.05 pH units using Whatman NBS grade buffers. The experiments were then gently agitated at room temperature (20 °C) for 48 h. After agitating, the final pH was measured, and the suspensions were separated via centrifugation at 2000*g* for 15 min. The resulting supernatants were filtered with 0.2 μM syringe filters, acidified with 1% HCl and analysed for Ni by inductively coupled plasma mass spectrometry (ICP-MS) with a Thermo iCAP Qc ion-coupled plasma mass spectrometer. Each data point was repeated in triplicate, with the largest standard deviation of ±2%.

2.3. Desorption experiments

Desorption experiments were performed with two sequential washes, first using ultrapure water and then using 0.01 M HCl (Curti et al., 2021; Kaiser and Guggenberger, 2007; Mikutta et al., 2005). The aim of the ultrapure water wash is to desorb Ni that is present as an outer-sphere complex on the surface, and we operationally define the Ni desorbed from this wash as 'weakly-bound' Ni. The aim of the dilute acid wash is to desorb Ni that is present as an inner-sphere complex on the surface, and we operationally define the Ni desorbed from this wash as 'strongly-bound' Ni.

The adsorption experiments described above were repeated at pH 8. After removal of the background electrolyte supernatant via centrifugation, 200 mL of ultrapure water at pH 8 was added to the centrifuge bottles. After gently agitating at room temperature for 48 h, the final pH was measured, the suspension was centrifuged and the supernatant was collected. Then 200 mL of 0.01 M HCl was added to the centrifuge bottles. Again after gently agitating at room temperature for 48 h, the final pH was measured, the suspension was centrifuged and the supernatant was collected. Supernatant wash solutions were filtered with 0.2 μM syringe filters, acidified with 1% HCl and analysed for Ni by ICP-MS using a Thermo iCAP Qc ion-coupled plasma mass spectrometer (ICP-MS). All desorption experiments were performed in triplicate.

2.4. Surface complexation modelling

pH adsorption edge data were fit using the thermodynamic surface complexation modelling program EQLFOR (Sherman, 2009). The basic Stern model (Westall and Hohl, 1980) was used to account for the surface electrostatics with a 2-site 1-pK formalism for protonation of the mineral surface, involving singly-coordinated ($\equiv MnOH^{-0.33}$) and doubly-coordinated surface oxygens ($\equiv Mn_2O^{-0.67}$) (Peacock and Sherman, 2007a):

$$\equiv MnOH^{-0.33} + H^+ = \equiv MnOH^{+0.67} \qquad logK_{MnOH} \qquad (1)$$

$$\equiv Mn_2O^{-0.67} + H^+ = \equiv Mn_2OH^{+0.33} \qquad logK_{Mn2O} \qquad (2)$$

The model input parameters for the binding constants for protonation of the mineral functional groups ($logK_{MnOH}$, $logK_{Mn2O}$), binding constants for electrolyte ions associating with these mineral groups, site densities of the mineral groups and capacitance of the Stern layer were determined via potentiometric titration reported in Supplementary Information B and summarised in Table 1. The Ni adsorption complexes forming on the mineral groups were constrained by extended X-ray absorption fine structure (EXAFS) spectroscopy, where previous work shows that Ni^{2+} (aq) is adsorbed to the surface of δMnO$_2$ and c-disordered birnessite at Mn octahedral vacancy sites present in the phyllomanganate layers (Peacock, 2009; Peacock and Sherman, 2007a; Sorensen et al., 2020). For the organo-mineral birnessite and following previous work for the adsorption of metals to similar organo-mineral (oxyhydr)oxides (Fariña et al., 2018; Moon and Peacock, 2012; Zhao et al., 2023), the Ni adsorption complexes were allowed to form on the mineral groups and on the carboxylic acid groups present at the mineral surface, which provide an additional adsorption site:

$$R - COO + H^+ = R - COOH \qquad logK_{R-COO} \qquad (3)$$
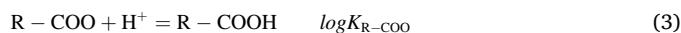
The Ni adsorption complexes forming on the carboxylic acid groups were constrained by near edge X-ray absorption fine structure (NEXAFS) spectroscopy, where previous work shows that butane 1, 2, 4 tricarboxylic acid adsorbs to organo-mineral (oxyhydr)oxides via two of its three carboxyl groups, thus leaving one carboxyl group available for adsorption of metals (Curti et al., 2021; Zhao et al., 2022). To represent the protonation of this carboxyl group the binding constants for protonation of the carboxylic acid groups were calculated for butane 1, 2, 4 tricarboxylic acid using the ACD/I-Lab 2.0 software (ACD/I-Lab, version 2.0, Advanced Chemistry Development, Inc) at pKa of 4.31, 4.82 and 5.21 and an average was taken of 4.78. The binding constant for the electrolyte ions associated with the carboxyl group was taken from fitted potentiometric titration data of *Bacillus subtilis*, in which the carboxyl group is shown to be the dominant surface site for metal adsorption (Moon and Peacock, 2013).

The site densities of the mineral groups for the organo-mineral birnessite were estimated using the site densities of the mineral groups for

Table 1

Parameters for the surface complexation model for adsorption of Ni and carboxylic acid on δMnO_2, c-disordered birnessite (Bn) and organo-birnessite (Org-b).

		δMnO_2	Bn	Org-b
wt% C				1.4[a]
Surface area (m^2/g)		188.2[b]	147.1[b]	166.4[b]
$\equiv MnOH^{-0.33}$ (mol/g)[c]		1.95×10^{-3}	1.95×10^{-3}	1.89×10^{-3}*[d]
$\equiv Mn_2O^{-0.67}$ (mol/g)[c]		1.01×10^{-3}	1.01×10^{-3}	9.77×10^{-4}*[d]
C_{stern} (F/m^2)		1.0[c]	1.0[c]	1.0[c]
Log K_{MnOH}	$\equiv MnOH^{-0.33} + H^+ = \equiv MnOH_2^{+0.33}$	3.36[c]	3.36[c]	3.36[c]
Log K_{MnOH_Na}	$\equiv MnOH^{-0.33} + Na^+ = \equiv MnOH^{-0.33}\text{-}Na^+$	−0.5[c]	−0.5[c]	−0.5[c]
Log K_{MnOH_Cl}	$\equiv MnOH^{-0.33} + H^+ + Cl^- = \equiv MnOH_2^{+0.33}\text{-}Cl^-$	2.86[c]	2.86[c]	2.86[c]
Log K_{Mn2O}	$\equiv Mn_2O^{-0.67} + H^+ = \equiv Mn_2OH^{+0.33}$	3.36[c]	3.36[c]	3.36[c]
Log K_{Mn2O_Na}	$\equiv Mn_2O^{-0.67} + Na^+ = \equiv Mn_2O^{-0.67}\text{-}Na^+$	−0.5[c]	−0.5[c]	−0.5[c]
Log K_{Mn2O_Cl}	$\equiv Mn_2O^{-0.67} + H^+ + Cl^- = \equiv Mn_2OH^{+0.33}\text{-}Cl^-$	2.86[c]	2.86[c]	2.86[c]
Log K_{COO}	$RCOO^- + H^+ = RCOOH$	4.78[e]	4.78[e]	4.78[e]
Log K_{COO_Na}	$RCOO^- + H^+ = RCOOH\text{-}Na^+$	−1.00[f]	−1.00[f]	−1.00[f]

[a] Measured by LECO;

[b] Measured by BET;

[c] Determined from potentiometric titration data.

[d] Calculated using the surface site densities of the pure birnessite weighted to the mineral:OC mass ratio of each composite;

[e] Calculated using ACD/I-Lab 2.0 (ACD/I-Lab, version 2.0, Advanced Chemistry Development, Inc).

[f] From Moon and Peacock (2013).

pure c-disordered birnessite weighted to the mineral:OC mass ratio (Table 1 and Supplementary Table A1). The total number of carboxyl groups available for trace metal sorption was estimated from the total wt % C measured for the organo-mineral and assuming two of its three carboxyl groups are adsorbed to the mineral (Supplementary Table A2).

3. Results

3.1. pH adsorption edge experiments

The Ni^{2+} (aq), NiCl$^+$ (aq) and Ni-formate$^+$ (aq) pH adsorption edge experiments with δMnO_2, c-disordered birnessite and organo-birnessite are shown in Fig. 1. All adsorption edges display a sigmoidal shape and pH-dependent adsorption, in which adsorption increases with increasing pH, in agreement with previous work for adsorption of Ni^{2+} (aq) (Peacock and Sherman, 2007a; Peña et al., 2010). The Ni^{2+} (aq), NiCl$^+$ (aq) and Ni-formate$^+$ (aq) adsorption edge experiments are similar regardless of the mineral crystallinity (Supplementary Fig. A3) but show varying adsorption behaviour dependent on the Ni solution speciation. For δMnO_2 and c-disordered birnessite, adsorption as a function of pH generally increases from least adsorption in the Ni-formate$^+$ (aq) adsorption experiments (pH$_{50}$ = ~6.4; where pH$_{50}$ is the pH at 50% adsorption), to intermediate adsorption in the NiCl$^+$ (aq) adsorption experiments (pH$_{50}$ = ~5.6), followed by most adsorption in the Ni^{2+} (aq) adsorption experiments (pH$_{50}$ = ~5.6 for δMnO_2; ~4.8 for c-
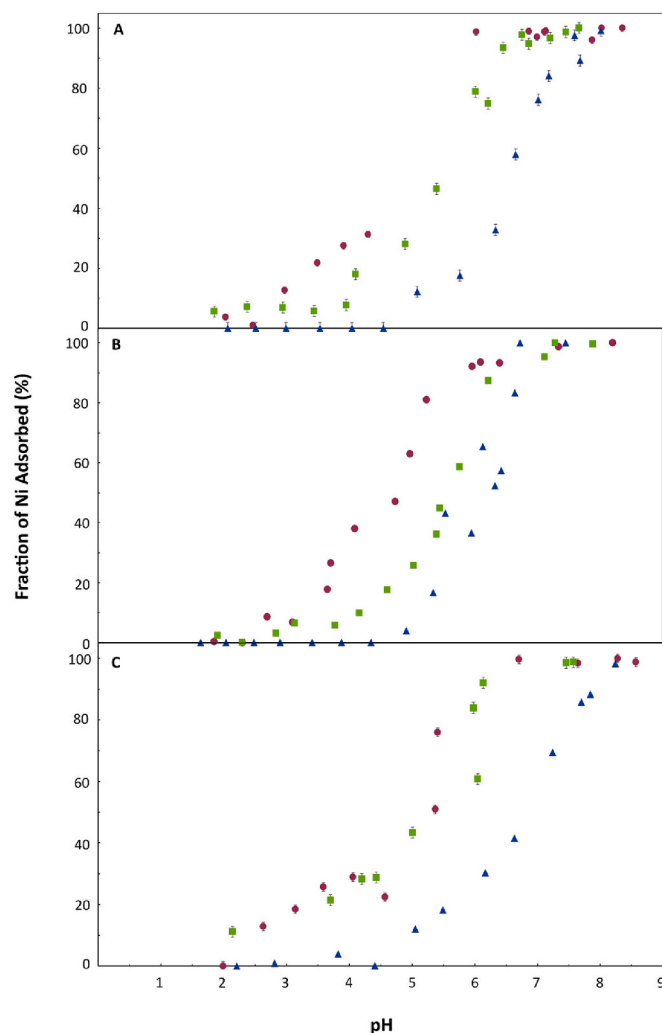

Fig. 1. Ni^{2+} (aq) (purple circles), NiCl$^+$ (aq) (green squares) and Ni-formate$^+$ (aq) (blue triangles) pH adsorption edge experiments with δMnO_2 (A), c-disordered birnessite (B) and organo-birnessite (C). Data points and error bars represent the mean and standard deviation of the mean for triplicate measurements. Where error bars are not visible this indicates that the uncertainty is smaller than the data point. (For interpretation of the references to colour in this figure legend, the reader is referred to the web version of this article.)

disordered birnessite). For organo-birnessite, adsorption as a function of pH increases from least adsorption in the Ni-formate$^+$ (aq) adsorption experiment (pH$_{50}$ = ~6.9), to most and similar adsorption in the Ni^{2+} (aq) and NiCl$^+$ (aq) adsorption experiments (pH$_{50}$ = ~5.4).

3.2. Desorption experiments

The desorption data show that negligible Ni is desorbed during the ultrapure water wash in any of the experiments (Supplementary Fig. A4), while variable Ni is desorbed during the acid wash in all experiments as shown in Fig. 2. For δMnO_2 and c-disordered birnessite, desorption at pH 8 is lowest in both the Ni^{2+} (aq) and NiCl$^+$ (aq) adsorption experiments (60 ± 3% and 51 ± 10% Ni desorbed with δMnO_2, respectively; 42 ± 11% and 41 ± 17% Ni desorbed with c-disordered birnessite, respectively), compared to the Ni-formate$^+$ (aq) adsorption experiments (70 ± 1% Ni desorbed with δMnO_2; 65 ± 3% Ni desorbed with c-disordered birnessite). For organo-birnessite, desorption at pH 8 is similar in all three adsorption experiments and is significantly higher than with δMnO_2 and c-disordered birnessite (75 ± 5%, 71 ± 3% and 65 ± 8% for Ni as speciated in the Ni^{2+} (aq), NiCl$^+$
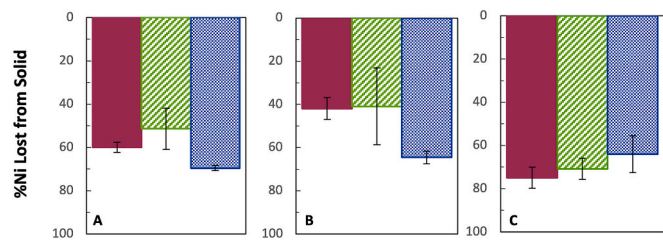
Fig. 2. Ni^{2+} (aq) (purple), $NiCl^+$ (aq) (green lined) and Ni-formate$^+$ (aq) (blue dotted) desorption from δMnO_2 (A), c-disordered birnessite (B) and organo-birnessite (C) with 0.01 M HCl acid wash. Bar columns and error bars represent the mean and standard deviation of the mean for triplicate measurements. Because negligible Ni is desorbed during the ultrapure water wash, this figure essentially shows the proportion of the total solid Ni that is desorbed (bar columns), and thus by mass balance the proportion of the total solid Ni that remains adsorbed (100% - bar columns). (For interpretation of the references to colour in this figure legend, the reader is referred to the web version of this article.)

(aq) and Ni-formate$^+$ (aq) adsorption experiments, respectively).

3.3. Surface complexation modelling

Spectroscopic evidence shows that Ni is sorbed to variably crystalline phyllomanganate as a surface adsorbed triple corner-sharing complex above/below vacancy sites or a structurally incorporated complex in vacancy sites in the phyllomanganate layers (Bodeï et al., 2007; Manceau et al., 2002; Peacock and Sherman, 2007a; Peña et al., 2010). Previous work shows that after 48 h, there is negligible incorporation of Ni into vacancy sites (Peacock, 2009; Peacock and Sherman, 2007a). Therefore, as the duration of our adsorption experiments was also 48 h, we expect there is similarly negligible incorporation of Ni into vacancy sites and, as such, a surface complexation model is appropriate to evaluate Ni binding affinity. For experiments using the organo-birnessite, Ni can also be complexed to carboxyl groups present at the mineral-water interface. The model fitted data is shown in Fig. 3 and model generated log K values in Table 2.

In the experiments, there is the complete adsorption of Ni at pH 8. Therefore, all solution species present are adsorbed to the mineral. In general, as Ni^{2+} is the dominant species in solution (Supplementary Fig. A2), the model predicts that $(\equiv Mn_2O)_3Ni^0$ is therefore also the

dominant surface species for all experiments and at all pH. For the minerals c-disordered birnessite and δMnO_2, in the Ni^{2+} (aq) adsorption experiments, $(\equiv Mn_2O)_3Ni^0$ is the sole surface species present, which is expected due to the low proportion of $NiCl^+$ (aq) in solution. In the $NiCl^+$ (aq) adsorption experiments, $(\equiv Mn_2O)_3NiCl^{-1}$ is present at the surface from pH 5 to 6. At pH 8, ~30% of total surface Ni is the $(\equiv Mn_2O)_3NiCl^{-1}$ surface species. In the Ni-Formate$^+$ (aq) adsorption experiments, $(\equiv Mn_2O)_3NiFA^{-1}$ (Ni-formate$^+$ adsorbed complex) is present at the surface at pH 6. At pH 8, ~25% of total surface Ni is the $(\equiv Mn_2O)_3NiFA^{-1}$ surface species. Both $(\equiv Mn_2O)_3NiCl^{-1}$ and $(\equiv Mn_2O)_3NiFA^{-1}$ surface species appear at higher pH than $(\equiv Mn_2O)_3Ni^0$ due to the negative charge from the chloride and formate ion, which is distributed to the outer electrostatic surface plane (Table 2).

For the organo-birnessite, in the Ni^{2+} (aq) adsorption experiments, binding of Ni to the carboxyl groups is present at pH 5 and at pH 8 increases to ~30% of total surface Ni. In the $NiCl^+$ (aq) adsorption experiments the $RCOO-Ni^{2+}$ and $(\equiv Mn_2O)_3NiCl^{-1}$ complexes are present from pH 5 to 6 and at pH 8 increase to ~20% of total surface Ni. In the Ni-Formate$^+$ (aq) adsorption experiments, the $RCOO-Ni^{2+}$ and $(\equiv Mn_2O)_3NiFA^{-1}$ complexes are present from pH 6 to 7 and at pH 8 increase to ~15% of total surface Ni.

4. Discussion

The adsorption results for δMnO_2 and c-disordered birnessite show that adsorption as a function of pH generally increases in the differently speciated adsorption experiments in the order of Ni-formate$^+$ (aq) experiments < $NiCl^+$ (aq) experiments < Ni^{2+} (aq) experiments (Fig. 1). This trend suggests that the average binding affinity of Ni in our adsorption experiments increases from the Ni-formate$^+$ (aq) experiments to the $NiCl^+$ (aq) experiments to the Ni^{2+} (aq) experiments, and thus that the binding affinity of the different Ni species increases in the order of Ni-formate$^+$ (aq) < $NiCl^+$ (aq) < Ni^{2+} (aq). Accordingly the surface complexation modelling for δMnO_2 and c-disordered birnessite shows that the binding affinity of Ni^{2+} (aq) in the Ni^{2+} (aq) adsorption experiments is fit with the highest stability constant (log K = 3.9 for δMnO_2; log K = 3.2 for c-disordered birnessite), followed by that for $NiCl^+$ (aq) in the $NiCl^+$ (aq) adsorption experiments (log K = 0.9 for δMnO_2; log K = 0.8 for c-disordered birnessite), followed by that for Ni-formate$^+$ (aq) in the Ni-formate$^+$ (aq) adsorption experiments (log K = 0.6 for δMnO_2; log K = 0.2 for c-disordered birnessite) (Table 2).
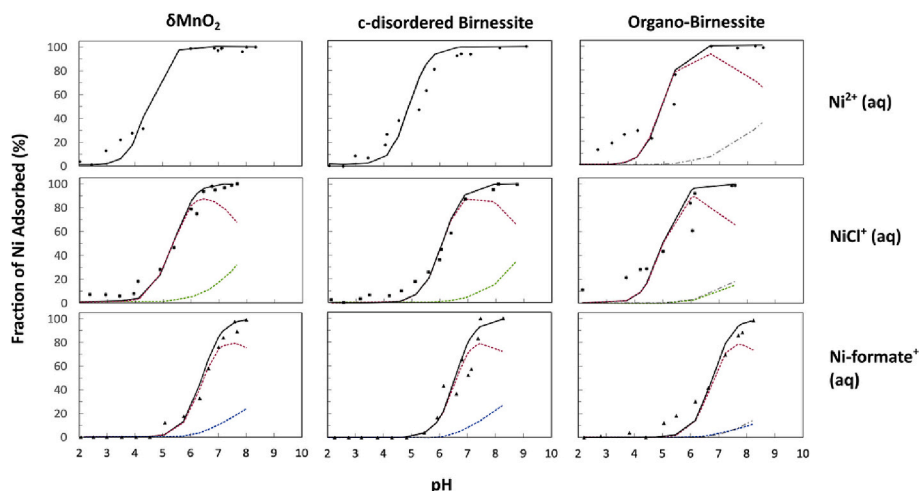

Fig. 3. Surface complexation model fits to the Ni^{2+} (aq), $NiCl^+$ (aq) and Ni-formate$^+$ (aq) pH adsorption edge experiments with δMnO_2, c-disordered birnessite and organo-birnessite. Experimental data (black symbols), total Ni adsorbed (black line), Ni^{2+} adsorbed complex ($(\equiv Mn_2O)_3$ Ni^0, purple line), $NiCl^+$ adsorbed complex ($(\equiv Mn_2O)_3$ $NiCl^{-1}$, green line), Ni-formate$^+$ adsorbed complex ($(\equiv Mn_2O)_3$ $NiFA^{-1}$, blue line) and Ni-carboxyl adsorbed complex ($RCOO-Ni^{2+}$, black dotted line). Data symbols represent the mean for triplicate measurements. Error bars that represent the standard deviation of the mean are not visible because the uncertainty is smaller than the data point. (For interpretation of the references to colour in this figure legend, the reader is referred to the web version of this article.)

Table 2
Log K and charge distribution for Ni species sorbed to δMnO$_2$, c-disordered birnessite (Bn), and organo-birnessite (Org-b).

Phase	Background Electrolyte	Complex	Log K	Δz$_0$	Δz$_1$
δMnO$_2$	Ni^{2+} (aq)	$3 \equiv Mn_2O^{-0.67} + Ni = (\equiv Mn_2O)_3Ni^0$	3.9	1.3	0.7
	NiCl$^+$ (aq)	$3 \equiv Mn_2O^{-0.67} + Ni = (\equiv Mn_2O)_3Ni^0$	3.5	1.3	0.7
		$3 \equiv Mn_2O^{-0.67} + NiCl^+ = (\equiv Mn_2O)_3NiCl^{-1}$	0.9	2	−1
	Ni-formate$^+$ (aq)	$3 \equiv Mn_2O^{-0.67} + Ni = (\equiv Mn_2O)_3Ni^0$	1.4	1.3	0.7
		$3 \equiv Mn_2O^{-0.67} + NiFA^+ = (\equiv Mn_2O)_3NiFA^{-1}$	0.6	1.9	−0.9
Bn	Ni^{2+} (aq)	$3 \equiv Mn_2O^{-0.67} + Ni = (\equiv Mn_2O)_3Ni^0$	3.2	1.3	0.7
	NiCl$^+$ (aq)	$3 \equiv Mn_2O^{-0.67} + Ni = (\equiv Mn_2O)_3Ni^0$	2.5	1.3	0.7
		$3 \equiv Mn_2O^{-0.67} + NiCl^+ = (\equiv Mn_2O)_3NiCl^{-1}$	0.8	2	−1
	Ni-formate$^+$ (aq)	$3 \equiv Mn_2O^{-0.67} + Ni = (\equiv Mn_2O)_3Ni^0$	1.2	1.3	0.7
		$3 \equiv Mn_2O^{-0.67} + NiFA^+ = (\equiv Mn_2O)_3NiFA^{-1}$	0.2	1.9	−0.9
Org-b	Ni^{2+} (aq)	$3 \equiv Mn_2O^{-0.67} + Ni = (\equiv Mn_2O)_3Ni^0$	3.1	1.3	0.7
		R-COO + Ni = RCOO-Ni^{2+}	2.1	2	0
	NiCl$^+$ (aq)	$3 \equiv Mn_2O^{-0.67} + Ni = (\equiv Mn_2O)_3Ni^0$	3.8	1.3	0.7
		$3 \equiv Mn_2O^{-0.67} + NiCl^+ = (\equiv Mn_2O)_3NiCl^{-1}$	0.8	2	−1
		R-COO + Ni = RCOO-Ni^{2+}	2.4	2	0
	Ni-formate$^+$ (aq)	$3 \equiv Mn_2O^{-0.67} + Ni = (\equiv Mn_2O)_3Ni^0$	1.0	1.3	0.7
		$3 \equiv Mn_2O^{-0.67} + NiFA^+ = (\equiv Mn_2O)_3NiFA^{-1}$	−0.4	1.9	−0.9
		R-COO + Ni = RCOO-Ni^{2+}	−0.4	2	0

Δz$_0$ and Δz$_1$ represent the charge distribution of the 0-plane and 1-plane respectively.

The adsorption results for organo-birnessite show that adsorption as a function of pH increases in the differently speciated adsorption experiments similarly to δMnO$_2$ and c-disordered birnessite in the order of Ni-formate$^+$ (aq) experiments < NiCl$^+$ (aq) experiments ~ Ni^{2+} (aq) experiments (Fig. 1). This trend again suggests that the average binding affinity of Ni in these adsorption experiments increases from the Ni-formate$^+$ (aq) experiment to the NiCl$^+$ (aq) and Ni^{2+} (aq) experiments, and thus that the binding affinity of the different Ni species increases in the order of Ni-formate$^+$ (aq) < NiCl$^+$ (aq) ~ Ni^{2+} (aq). The surface complexation modelling for organo-birnessite predicts that the Ni^{2+} (aq) species present in all three adsorption experiments adsorbs to the carboxyl groups present at the organo-birnessite surface, in agreement with previous work (Boonfueng et al., 2009; Fariña et al., 2018; Moon and Peacock, 2012), where at pH ~8 the adsorbed Ni in the Ni^{2+} (aq) adsorption experiments is comprised of ~60% Ni^{2+} complexes and ~ 40% Ni^{2+} adsorbed to carboxyl groups (RCOO-Ni^{2+}); while the NiCl$^+$ (aq) adsorption experiments feature ~20% Ni-carboxyl complexes and ~ 20% NiCl$^+$ complexes, and the Ni-formate$^+$ (aq) adsorption experiments feature ~15% Ni-carboxyl complexes and ~ 15% Ni-formate$^+$ complexes (Fig. 3, Table 2).

The desorption results for δMnO$_2$ and c-disordered birnessite at pH 8 show that desorption is non quantitative and increases in the order of Ni-formate$^+$ (aq) experiments > NiCl$^+$ (aq) experiments ~ Ni^{2+} (aq) experiments (Fig. 2). This trend suggests that the average bonding strength increases from the Ni-formate$^+$ (aq) experiments to the NiCl$^+$ (aq) experiments and the Ni^{2+} (aq) experiments, and thus that the bonding strength of the different Ni species increases in the order of Ni-formate$^+$ (aq) < NiCl$^+$ (aq) ~ Ni^{2+} (aq). The desorption results for organo-birnessite at pH 8 show that desorption is non quantitative and similar for all three experiments, and generally higher than for δMnO$_2$ and c-disordered birnessite, suggesting that the average bonding strength is similar in these experiments and decreased by the presence of the organic carbon at the birnessite mineral surface. Taken together the Ni-formate$^+$ (aq) and Ni organo-birnessite desorption experiments suggest that Ni bonding strength is decreased by the presence of the organic carbon, compared to NiCl$^+$ (aq) and Ni^{2+} (aq).

It should be noted that our bonding strength assignations are inferred from desorption experiments performed over a fixed time period to provide an operationally defined measure of bonding strength based on the relative desorbability of the Ni complexes. Although our adsorption and desorption experiments were both run for 48 h, previous work shows that desorption can be slower than adsorption (e.g., McBride, 1989; Backes et al., 1995) and as such, a longer desorption period may result in further Ni loss to solution and thus greater adsorption reversibility. The Ni molecular-level bonding environments of Ni^{2+} (aq), NiCl$^+$ (aq) and Ni-formate$^+$ (aq) on phyllomanganate, and of Ni in Ni-organo-birnessite complexes, could provide an independent measure of bonding strength, but not all of these have been determined, and those that have are measured under different experimental conditions and on phyllomanganates of varying crystallinity from abiotic and biotic syntheses. None-the-less, EXAFS spectroscopy shows that the Ni molecular-level bonding environment of Ni^{2+} (aq) adsorbed at vacancy sites on phyllomanganate consists of ~6 oxygens with an average Ni-O bond length of 2.04–2.05 Å (e.g., Peacock and Sherman, 2007a; Peacock, 2009; Peña et al., 2010; Sorensen et al., 2020), while Ni complexed with the biomass component of bacteriogenic phyllomanganate consists of ~6 oxygens with an average Ni-O bond length of 2.06 Å (Peña et al., 2011); and Ni complexed with carboxylic acids and humic substances has average Ni-O bond lengths at 2.03–2.05 Å and 2.04–2.10 Å, respectively (Strathmann and Myneni, 2004; Xia et al., 1997). Uncertainties on EXAFS-derived bond lengths are often cited from <0.005 Å up to ±0.05 Å, but these previous works appear to broadly support that, compared to Ni^{2+} (aq) complexes, Ni-organic complexes might have somewhat longer Ni-O bond lengths in their immediate coordination environment, such that in these complexes the Ni bonding strength is decreased.

Given that during equilibrium stable isotope fractionation heavy Ni isotopes should concentrate in bonding environments that provide relatively increased bonding strength, while lighter Ni isotopes should concentrate in bonding environments that provide relatively decreased binding strength (e.g., Schauble, 2004), our desorption results suggest that Ni in Ni^{2+} (aq) and NiCl$^+$ (aq) adsorbed complexes should be isotopically heaviest while Ni in an Ni-organic ligand or Ni adsorbed onto organo-birnessite should be isotopically lightest (Fig. 4). Whilst our Ni^{2+} (aq), NiCl$^+$ (aq) and Ni-formate$^+$ (aq) adsorption experiments cannot capture the complexities of Ni adsorption to phyllomanganates in sediments, they do mimic the dominant inorganic speciation and an organic ligand speciation of Ni in seawater (Turner et al., 1981; Barcelona, 1980), respectively, and their adsorption to the dominant phyllomanganate phases found in sediments (Manceau et al., 2014; Peacock, 2009; Peacock and Sherman, 2007a, 2007b). As such these results suggest that the presence of organic carbon could influence Ni isotope fractionation in marine sediments. Fe–Mn crusts have very low total organic carbon (TOC), as they are not precipitated in the sediment column and are thus not exposed to elevated dissolved organic carbon in porewaters (Barcelona, 1980; Burdige and Komada, 2015). They are also the isotopically heaviest Mn-rich deposits in marine settings, with an
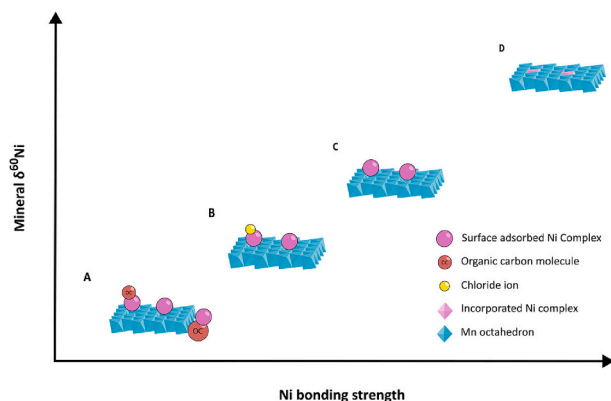
Fig. 4. Schematic diagram showing the relationship between Ni bonding strength and predictions for $\delta^{60}Ni$ for various Ni species bonded to variably crystalline phyllomanganate / organo-phyllomanganate minerals. Mineral complexes A, B and C represent three different Ni speciation scenarios investigated in the experiments: A is an organic rich endmember in which Ni is adsorbed as an Ni-organic ligand and as Ni^{2+} (aq) bound to organic matter on the mineral; B represents Ni^{2+} (aq) and $NiCl^+$ (aq) adsorbed to the mineral vacancy sites; and C represents solely Ni^{2+} (aq) adsorbed to the mineral vacancy sites. D shows Ni entirely incorporated into the mineral structure, which should provide the highest bonding strength for Ni as it occupies a lower energy state (Peña et al., 2010) and therefore likely the isotopically heaviest mineral $\delta^{60}Ni$ compared to the different speciation scenarios.

average Ni isotope composition of $+1.55 \pm 0.38‰$, which is identical within error to seawater which has an average Ni isotope composition of $1.33 \pm 0.13‰$ (Cameron and Vance, 2014; Gall et al., 2013; Gueguen et al., 2021; Gueguen et al., 2016). Contrastingly, pelagic sediments are exposed to organic ligands in porewaters and Ni in these settings is likely adsorbed in the presence of organics (Barcelona, 1980; Burdige and Komada, 2015; Papadimitriou et al., 2002). Although the organic complexes present in porewaters are more complex and varied than those presented in this study, pelagic sediments indeed have lighter Ni isotope compositions than ferromanganese crusts ranging from $+0.26$ to $+1.08‰$ (Fleischmann et al., 2023; Gall et al., 2013). Sediments with enriched Mn and higher TOC concentrations compared to other pelagic sediments, such as the suboxic sediments from the California borderland basin have even lighter Ni isotope compositions ranging from -0.20 to $0.09‰$ (Fleischmann et al., 2023). Therefore, Ni isotope compositions of Mn-rich sediments could be influenced by the presence of organic carbon.

It is unlikely that Ni speciation is the sole control on Ni isotope compositions in Mn-rich sediments. There are several other physiochemical factors that may also influence the bond strength of Ni to phyllomanganates and therefore affect Ni isotope compositions. Notably the mechanism of uptake, either surface adsorption or structural incorporation, is likely an important factor influencing isotope compositions, as structural incorporation of Ni into vacancy sites provides a stronger bonding environment than surface adsorption (Peña et al., 2010) and is thus expected to favour heavy isotopes (e.g., Schauble, 2004) (Fig. 4). The essentially complete incorporation of Ni as observed in Fe–Mn crusts (Peacock and Sherman, 2007b) therefore also likely contributes to the heavy isotope composition observed in these deposits (Chen et al., 2022). More generally, the balance between Ni surface adsorption and incorporation into mineral vacancies could be an important factor governing the range of Ni isotope compositions in pelagic and suboxic sediments as well (Chen et al., 2022; Fleischmann et al., 2023). Therefore, the role of Ni speciation may add further variability to Ni isotope values in the marine environment.

5. Conclusion

Using adsorption and desorption experiments in conjunction with surface complexation modelling, this study investigates the binding affinity and bonding strength of different Ni aqueous complexes to phyllomanganates, namely Ni^{2+} (aq), $NiCl^+$ (aq) and Ni-formate$^+$ (aq) to δMnO_2, c-disordered birnessite and organo-mineral c-disordered birnessite. For δMnO_2 and c-disordered birnessite, adsorption increases in the order of Ni-formate$^+$ (aq) experiments < $NiCl^+$ (aq) experiments < Ni^{2+} (aq) experiments. Together with the surface complexation modelling this trend indicates that the binding affinity of the different Ni species increases in the order of Ni-formate$^+$ (aq) < $NiCl^+$ (aq) < Ni^{2+} (aq). Similarly, for organo-birnessite, our data indicates that the binding affinity of the different Ni species increases in the order of Ni-formate$^+$ (aq) < $NiCl^+$ (aq) ~ Ni^{2+} (aq) (Fig. 1). Accordingly, the surface complexation modelling predicts that Ni^{2+} (aq) adsorbs to carboxyl groups (RCOO-Ni^{2+}) and that these surface complexes have lower binding affinity relative to Ni species adsorbed directly to the mineral surface. For δMnO_2 and c-disordered birnessite, desorption increases in the opposite order compared to adsorption in the order of Ni-formate$^+$ (aq) > $NiCl^+$ (aq) ~ Ni^{2+} (aq), suggesting that the bonding strength increases in the order of Ni-formate$^+$ (aq) < $NiCl^+$ (aq) ~ Ni^{2+} (aq). While for organo-birmessite desorption is similar in all three experiments, and generally higher than for δMnO_2 and c-disordered birnessite, suggesting that the bonding strength is similar in these experiments and decreased by the presence of the organo-birnessite carboxyl groups that are located at the mineral surface.

Because bonding strength governs equilibrium stable isotope fractionation, the differences in bonding strength of Ni species to phyllomanganate suggest that different Ni species might have different isotope behaviours during adsorption. Specifically, Ni^{2+} (aq) and $NiCl^+$ (aq) appear to be the most strongly adsorbing species to δMnO_2 and c-disordered birnessite, and therefore their adsorbed complexes should be isotopically heaviest compared to adsorbed Ni-formate$^+$. In the presence of organics either in solution as Ni-formate$^+$ (aq) or on the mineral surfaces as an organo-birnessite, Ni appears to be weakly adsorbed. Thus, Ni adsorbed in the presence of organics should be isotopically light relative to Ni adsorbed in the absence of organics. These experimental results are consistent with the heavy isotope composition of Fe-Mn crusts, which have low TOC content, and the light isotope composition of Mn-rich sediments, which have high TOC content. We note that the role of Ni adsorption versus incorporation to the mineral may play an even greater role in explaining the variation in the Ni isotope composition in Mn-rich sediments, however, the work here suggests that Ni speciation and the presence of organics is a factor that can further increase the range of $\delta^{60}Ni$ values measured.

CRediT authorship contribution statement

Lena Chen: Writing – review & editing, Writing – original draft, Methodology, Investigation, Formal analysis, Conceptualization. **William B. Homoky:** Writing – review & editing, Validation, Supervision. **Caroline L. Peacock:** Writing – review & editing, Validation, Supervision, Methodology, Investigation, Conceptualization.

Declaration of competing interest

Lena Chen reports financial support was provided by Natural

Environment Research Council. Caroline L. Peacock reports financial support was provided by The Royal Society. If there are other authors, they declare that they have no known competing financial interests or personal relationships that could have appeared to influence the work reported in this paper.

Data availability

Data will be made available on request.

Acknowledgements

We thank laboratory managers Andrew Hobson and Stephen Reid, and laboratory technician Fiona Keay (University of Leeds) for laboratory support.

Appendix A. Supplementary data

Supplementary data to this article can be found online at https://doi.org/10.1016/j.chemgeo.2024.122067.

References

Anbar, A.D., 2008. Oceans: Elements and evolution. Science 1979 (322), 1481–1483. https://doi.org/10.1126/science.1163100.

Atkins, A.L., Shaw, S., Peacock, C.L., 2016. Release of Ni from birnessite during transformation of birnessite to todorokite: Implications for Ni cycling in marine sediments, vol. 189, pp. 158–183.

Backes, C.A., McLaren, R.G., Rate, A.W., Swift, R.S., 1995. Kinetics of Cadmium and Cobalt Desorption from Iron and Manganese Oxides. Soil Sci. Soc. Am. J. 59, 778–785. https://doi.org/10.2136/sssaj1995.03615995005900030021x.

Barcelona, M.J., 1980. Dissolved organic carbon and volatile fatty acids in marine sediment pore waters. Geochim. Cosmochim. Acta 44, 1977–1984. https://doi.org/10.1016/0016-7037(80)90197-0.

Barondeau, D.P., Kassmann, C.J., Bruns, C.K., Tainer, J.A., Getzoff, E.D., 2004. Nickel superoxide dismutase structure and mechanism. Biochemistry 43, 8038–8047. https://doi.org/10.1021/BI0496081/ASSET/IMAGES/LARGE/BI0496081F00006.JPEG.

Bodeï, S., Manceau, A., Geoffroy, N., Baronnet, A., Buatier, M., 2007. Formation of todorokite from vernadite in Ni-rich hemipelagic sediments. Geochim. Cosmochim. Acta 71, 5698–5716. https://doi.org/10.1016/J.GCA.2007.07.020.

Boonfueng, T., Axe, L., Yee, N., Hahn, D., Ndiba, P.K., 2009. Zn sorption mechanisms onto sheathed Leptothrix discophora and the impact of the nanoparticulate biogenic Mn oxide coating. J. Colloid Interface Sci. 333, 439–447. https://doi.org/10.1016/J.JCIS.2009.02.033.

Burdige, D.J., Komada, T., 2015. Sediment pore waters. In: Biogeochemistry of Marine Dissolved Organic Matter: Second Edition, 535–577. https://doi.org/10.1016/B978-0-12-405940-5.00012-1.

Cameron, V., Vance, D., 2014. Heavy nickel isotope compositions in rivers and the oceans. Geochim. Cosmochim. Acta 128, 195–211. https://doi.org/10.1016/J.GCA.2013.12.007.

Cameron, V., Vance, D., Archer, C., House, C.H., 2009. A biomarker based on the stable isotopes of nickel. Proc. Natl. Acad. Sci. USA 106, 10944–10948. https://doi.org/10.1073/pnas.0900726106.

Charlton, S.R., Parkhurst, D.L., 2002. PHREEQCI–A graphical user interface to the geochemical model PHREEQC. In: US Geological Survey.

Chen, L., Archer, C., Little, S.H., Peacock, C.L., 2022. An isotopically heavy source of nickel: Release of nickel during birnessite transformation into todorokite. In: in: 2022 Goldschmidt Conference. GOLDSCHMIDT.

Curti, L., Moore, O.W., Babakhani, P., Xiao, K.Q., Woulds, C., Bray, A.W., Fisher, B.J., Kazemian, M., Kaulich, B., Peacock, C.L., 2021. Carboxyl-richness controls organic carbon preservation during coprecipitation with iron (oxyhydr)oxides in the natural environment. Commun. Earth Environ. 1 (2), 1–13. https://doi.org/10.1038/s43247-021-00301-9.

Dupont, C.L., Buck, K.N., Palenik, B., Barbeau, K., 2010. Nickel utilization in phytoplankton assemblages from contrasting oceanic regimes. Deep-Sea Res. I Oceanogr. Res. Pap. 57, 553–566. https://doi.org/10.1016/J.DSR.2009.12.014.

Fariña, A.O., Peacock, C.L., Fiol, S., Antelo, J., Carvin, B., 2018. A universal adsorption behaviour for Cu uptake by iron (hydr)oxide organo-mineral composites. Chem. Geol. 479, 22–35. https://doi.org/10.1016/J.CHEMGEO.2017.12.022.

Fleischmann, S., Du, J., Chatterjee, A., McManus, J., Iyer, S.D., Amonkar, A., Vance, D., 2023. The nickel output to abyssal pelagic manganese oxides: a balanced elemental and isotope budget for the oceans. Earth Planet. Sci. Lett. 619, 118301 https://doi.org/10.1016/J.EPSL.2023.118301.

Fujii, T., Moynier, F., Dauphas, N., Abe, M., 2011. Theoretical and experimental investigation of nickel isotopic fractionation in species relevant to modern and ancient oceans. Geochim. Cosmochim. Acta 75, 469–482. https://doi.org/10.1016/J.GCA.2010.11.003.

Gall, L., Williams, H.M., Siebert, C., Halliday, A.N., Herrington, R.J., Hein, J.R., 2013. Nickel isotopic compositions of ferromanganese crusts and the constancy of deep ocean inputs and continental weathering effects over the Cenozoic. Earth Planet. Sci. Lett. 375, 148–155. https://doi.org/10.1016/j.epsl.2013.05.019.

Gueguen, B., Rouxel, O., 2021. The Nickel isotope composition of the authigenic sink and the diagenetic flux in modern oceans. Chem. Geol. 563, 120050 https://doi.org/10.1016/j.chemgeo.2020.120050.

Gueguen, B., Rouxel, O., Rouget, M.L., Bollinger, C., Ponzevera, E., Germain, Y., Fouquet, Y., 2016. Comparative geochemistry of four ferromanganese crusts from the Pacific Ocean and significance for the use of Ni isotopes as paleoceanographic tracers. Geochim. Cosmochim. Acta 189, 214–235. https://doi.org/10.1016/J.GCA.2016.06.005.

Gueguen, B., Rouxel, O., Fouquet, Y., 2021. Nickel isotopes and rare earth elements systematics in marine hydrogenetic and hydrothermal ferromanganese deposits. Chem. Geol. 560, 119999 https://doi.org/10.1016/J.CHEMGEO.2020.119999.

Homoky, W.B., Weber, T., Berelson, W.M., Conway, T.M., Henderson, G.M., Van Hulten, M., Jeandel, C., Severmann, S., Tagliabue, A., 2016. Quantifying trace element and isotope fluxes at the ocean sediment boundary: a review. Philos. Trans. R. Soc. A Math. Phys. Eng. Sci. 374 https://doi.org/10.1098/RSTA.2016.0246.

Horner, T.J., Little, S.H., Conway, T.M., Farmer, J.R., Hertzberg, J.E., Janssen, D.J., Lough, A.J.M., McKay, J.L., Tessin, A., Galer, S.J.G., Jaccard, S.L., Lacan, F., Paytan, A., Wuttig, K., 2021. Bioactive trace metals and their isotopes as paleoproductivity proxies: an assessment using GEOTRACES-Era data. Glob. Biogeochem. Cycles 35. https://doi.org/10.1029/2020GB006814 e2020GB006814.

Jaun, B., Thauer, R.K., 2007. Methyl-coenzyme M reductase and its nickel corphin coenzyme F430 in methanogenic archaea. In: Nickel and its Surprising Impact in Nature. John Wiley & Sons, Ltd, pp. 323–356. https://doi.org/10.1002/9780470028131.ch8.

Jiang, W., Saxena, A., Song, B., Ward, B.B., Beveridge, T.J., Myneni, S.C.B., 2004. Elucidation of Functional Groups on Gram-Positive and Gram-Negative Bacterial Surfaces Using Infrared Spectroscopy. https://doi.org/10.1021/LA049043.

John, S.G., Kelly, R.L., Bian, X., Fu, F., Smith, M.I., Lanning, N.T., Liang, H., Pasquier, B., Seelen, E.A., Holzer, M., Wasylenki, L., Conway, T.M., Fitzsimmons, J.N., Hutchins, D.A., Yang, S.C., 2022. The biogeochemical balance of oceanic nickel cycling. Nat. Geosci. 11 (15), 906–912. https://doi.org/10.1038/s41561-022-01045-7.

Kaiser, K., Guggenberger, G., 2007. Sorptive stabilization of organic matter by microporous goethite: sorption into small pores vs. surface complexation. Eur. J. Soil Sci. 58, 45–59. https://doi.org/10.1111/J.1365-2389.2006.00799.X.

Konhauser, K.O., Pecoits, E., Lalonde, S.V., Papineau, D., Nisbet, E.G., Barley, M.E., Arndt, N.T., Zahnle, K., Kamber, B.S., 2009. Oceanic nickel depletion and a methanogen famine before the Great Oxidation Event. Nature 458 (7239), 750–753. https://doi.org/10.1038/nature07858.

Konhauser, K.O., Robbins, L.J., Pecoits, E., Peacock, C., Kappler, A., Lalonde, S.V., 2015. The archean nickel famine revisited. Astrobiology 15, 804–815. https://doi.org/10.1089/AST.2015.1301/ASSET/IMAGES/LARGE/FIGURE2.JPEG.

Lemaitre, N., Du, J., de Souza, G.F., Archer, C., Vance, D., 2022. The essential bioactive role of nickel in the oceans: evidence from nickel isotopes. Earth Planet. Sci. Lett. 584, 117513 https://doi.org/10.1016/J.EPSL.2022.117513.

Little, S.H., Archer, C., McManus, J., Najorka, J., Wegorzewski, A.V., Vance, D., 2020. Towards balancing the oceanic Ni budget. Earth Planet. Sci. Lett. 547, 116461 https://doi.org/10.1016/j.epsl.2020.116461.

Manceau, A., Tamura, N., Marcus, M.A., MacDowell, A.A., Celestre, R.S., Sublett, R.E., Sposito, G., Padmore, H.A., 2002. Deciphering Ni sequestration in soil ferromanganese nodules by combining X-ray fluorescence, absorption, and diffraction at micrometer scales of resolution. Am. Mineral. 87, 1494–1499. https://doi.org/10.2138/AM-2002-1028.

Manceau, A., Lanson, M., Takahashi, Y., 2014. Mineralogy and crystal chemistry of Mn, Fe, Co, Ni, and Cu in a deep-sea Pacific polymetallic nodule. Am. Mineral. 99, 2068–2083. https://doi.org/10.2138/AM-2014-4742.

McBride, M.B., 1989. In: Stewart, B.A. (Ed.), Reactions Controlling Heavy Metal Solubility in Soils BT - Advances in Soil Science, vol. 10. Springer, New York, New York, NY, pp. 1–56. https://doi.org/10.1007/978-1-4613-8847-0_1.

Merroun, M.L., Nedelkova, M., Ojeda, J.J., Reitz, T., Fernández, M.L., Arias, J.M., Romero-González, M., Selenska-Pobell, S., 2011. Bio-precipitation of uranium by two bacterial isolates recovered from extreme environments as estimated by potentiometric titration, TEM and X-ray absorption spectroscopic analyses. J. Hazard. Mater. 197, 1–10. https://doi.org/10.1016/J.JHAZMAT.2011.09.049.

Mikutta, R., Kleber, M., Kaiser, K., Jahn, R., 2005. Review: organic matter removal from soils using hydrogen peroxide, sodium hypochlorite, and disodium peroxodisulfate. Soil Sci. Soc. Am. J. 69, 120–135. https://doi.org/10.2136/SSSAJ2005.0120.

Moon, E.M., Peacock, C.L., 2012. Adsorption of Cu(II) to ferrihydrite and ferrihydrite-bacteria composites: Importance of the carboxyl group for Cu mobility in natural environments. Geochim. Cosmochim. Acta 92, 203–219. https://doi.org/10.1016/j.gca.2012.06.012.

Moon, E.M., Peacock, C.L., 2013. Modelling Cu(II) adsorption to ferrihydrite and ferrihydrite–bacteria composites: Deviation from additive adsorption in the composite sorption system. Geochim. Cosmochim. Acta 104, 148–164. https://doi.org/10.1016/J.GCA.2012.11.030.

Papadimitriou, S., Kennedy, H., Bentaleb, I., Thomas, D.N., 2002. Dissolved organic carbon in sediments from the eastern North Atlantic. Mar. Chem. 79, 37–47. https://doi.org/10.1016/S0304-4203(02)00055-5.

Park, S., Kwon, K.D., 2021. Atomistic Insights into the Interlayer Cation and Water Structures of Na-, K-, and Cs-Birnessite. ACS Earth Space Chem. https://doi.org/10.1021/ACSEARTHSPACECHEM.1C00259 acsearthspacechem.1c00259.

Peacock, C.L., 2009. Physiochemical controls on the crystal-chemistry of Ni in birnessite: Genetic implications for ferromanganese precipitates. Geochim. Cosmochim. Acta 73, 3568–3578. https://doi.org/10.1016/J.GCA.2009.03.020.

Peacock, C.L., Sherman, D.M., 2007a. Sorption of Ni by birnessite: Equilibrium controls on Ni in seawater. Chem. Geol. 238, 94–106. https://doi.org/10.1016/j.chemgeo.2006.10.019.

Peacock, C.L., Sherman, D.M., 2007b. Crystal-chemistry of Ni in marine ferromanganese crusts nodules. Am. Mineral. 92, 1087–1092. https://doi.org/10.2138/am.2007.2378.

Peña, J., Kwon, K.D., Refson, K., Bargar, J.R., Sposito, G., 2010. Mechanisms of nickel sorption by a bacteriogenic birnessite. Geochim. Cosmochim. Acta 74, 3076–3089. https://doi.org/10.1016/j.gca.2010.02.035.

Ragsdale, S.W., 2009. Nickel-based enzyme systems. J. Biol. Chem. 284, 18571–18575. https://doi.org/10.1074/JBC.R900020200/ATTACHMENT/3D5F6A1D-3C3A-4FF2-A5AD-B2E0C5AB66ED/MMC1.PDF.

Schauble, E.A., 2004. Applying Stable Isotope Fractionation Theory to New Systems. Rev. Mineral. Geochem. 55, 65–111. https://doi.org/10.2138/GSRMG.55.1.65.

Sherman, D., 2009. Surface complexation modeling: Mineral fluid equilibria at the molecular scale. Thermodynam. Kinet. Water-Rock Interact. 181–206.

Sorensen, J.V., Gueguen, B., Stewart, B.D., Peña, J., Rouxel, O., Toner, B.M., 2020. Large nickel isotope fractionation caused by surface complexation reactions with hexagonal birnessite. Chem. Geol. 537, 119481 https://doi.org/10.1016/J.CHEMGEO.2020.119481.

Toner, B., Fakra, S., Villalobos, M., Warwick, T., Sposito, G., 2005a. Spatially resolved characterization of biogenic manganese oxide production within a bacterial biofilm. Appl. Environ. Microbiol. 71, 1300–1310. https://doi.org/10.1128/AEM.71.3.1300-1310.2005/ASSET/8AD201AE-A2C9-4306-B0AA-A87120D90375/ASSETS/GRAPHIC/ZAM0030552810007.JPEG.

Toner, B., Manceau, A., Marcus, M.A., Millet, D.B., Sposito, G., 2005b. Zinc Sorption by a Bacterial Biofilm. Environ. Sci. Technol. 39, 8288–8294. https://doi.org/10.1021/es050528+.

Turner, A., Martino, M., 2006. Modelling the equilibrium speciation of nickel in the Tweed Estuary, UK: Voltammetric determinations and simulations using WHAM. Mar. Chem. 102, 198–207. https://doi.org/10.1016/J.MARCHEM.2006.04.002.

Turner, D.R., Whitfield, M., Dickson, A.G., 1981. The equilibrium speciation of dissolved components in freshwater and sea water at 25°C and 1 atm pressure. Geochim. Cosmochim. Acta 45, 855–881. https://doi.org/10.1016/0016-7037(81)90115-0.

Villalobos, M., Toner, B., Bargar, J., Sposito, G., 2003. Characterization of the manganese oxide produced by Pseudomonas putida strain MnB1. Geochim. Cosmochim. Acta 67, 2649–2662. https://doi.org/10.1016/S0016-7037(03)00217-5.

Vraspir, J.M., Butler, A., 2009. Chemistry of Marine Ligands and Siderophores. Annu. Rev. Mar. Sci. 1, 43. https://doi.org/10.1146/ANNUREV.MARINE.010908.163712.

Wang, S.J., Rudnick, R.L., Gaschnig, R.M., Wang, H., Wasylenki, L.E., 2019. Methanogenesis sustained by sulfide weathering during the Great Oxidation Event. Nat. Geosci. 4 (12), 296–300. https://doi.org/10.1038/s41561-019-0320-z.

Warren, L.A., Haack, E.A., 2001. Biogeochemical controls on metal behaviour in freshwater environments. Earth Sci. Rev. 54, 261–320. https://doi.org/10.1016/S0012-8252(01)00032-0.

Westall, J., Hohl, H., 1980. A comparison of electrostatic models for the oxide/solution interface. Adv. Colloid Interf. Sci. 12, 265–294. https://doi.org/10.1016/0001-8686(80)80012-1.

Zark, M., Dittmar, T., 2018. Universal molecular structures in natural dissolved organic matter. Nat. Commun. 9, 3178. https://doi.org/10.1038/s41467-018-05665-9.

Zhang, M., Peacock, C.L., Cai, P., Xiao, K.Q., Qu, C., Wu, Y., Huang, Q., 2021. Selective retention of extracellular polymeric substances induced by adsorption to and coprecipitation with ferrihydrite. Geochim. Cosmochim. Acta 299, 15–34. https://doi.org/10.1016/J.GCA.2021.02.015.

Zhao, Y., Moore, O.W., Xiao, K.Q., Curti, L., Fariña, A.O., Banwart, S.A., Peacock, C.L., 2022. The role and fate of organic carbon during aging of ferrihydrite. Geochim. Cosmochim. Acta 335, 339–355. https://doi.org/10.1016/J.GCA.2022.07.003.

Zhao, Y., Otero-Fariña, A., Xiao, K.Q., Moore, O.W., Banwart, S.A., Ma, F.J., Gu, Q.B., Peacock, C.L., 2023. The mobility and fate of Cr during aging of ferrihydrite and ferrihydrite organominerals. Geochim. Cosmochim. Acta 347, 58–71. https://doi.org/10.1016/J.GCA.2023.02.021.